

# Rib waveguides for Kerr nonlinear optics



Citation for the original published paper (version of record):

Shekhawat, V., Zhao, P., Lindvall, N. et al (2025). Rib waveguides for Kerr nonlinear optics. Optics Express, 33(24): 50811-50821. http://dx.doi.org/10.1364/OE.574369

N.B. When citing this work, cite the original published paper.

research.chalmers.se offers the possibility of retrieving research publications produced at Chalmers University of Technology. It covers all kind of research output: articles, dissertations, conference papers, reports etc. since 2004. research.chalmers.se is administrated and maintained by Chalmers Library

## Rib waveguides for Kerr nonlinear optics

VIJAY SHEKHAWAT,1,\* D PING ZHAO,2 D NICLAS LINDVALL,1 MARCELLO GIRARDI, 1,3 PETER A. ANDREKSON, 1 D AND VICTOR TORRES-COMPANY 1

**Abstract:** Optical amplifiers are fundamental to high-throughput optical communication systems, but traditional rare-earth-doped amplifiers with limited optical bandwidth increasingly constrain the scalability of next-generation fiber networks. Integrated optical parametric amplifiers (OPAs), based on Kerr nonlinear optics, are potential candidates to address this challenge by offering broadband gain across arbitrary wavelengths when they are operated in an un-depleted pump regime with available low-noise pump lasers. However, their performance is currently limited by optical losses in meter-scale waveguides, which limits the maximum achievable gain. In this work, we challenge the conventional preference for strip waveguides in Kerr-based systems and demonstrate with numerical studies that at the maximum effective length rib waveguides fabricated on the silicon nitride (Si<sub>3</sub>N<sub>4</sub>) platform can offer substantially higher gain, despite a lower effective nonlinear coefficient. This comes at the cost of longer length, which we address using a meander-style spiral concatenation, and we also show how to avoid active stitching error compensation in electron-beam lithography during the fabrication of these meter-long waveguides. We further investigate the fabrication tolerance of group velocity dispersion in both geometries and show that rib waveguides maintain comparable performance. These results pave the way not only for practical OPAs but also for other devices based on  $\chi^{(3)}$  nonlinearity such as wavelength converters and optical sampling oscilloscopes by simultaneously providing high gain, broad bandwidth, and a low noise figure.

Published by Optica Publishing Group under the terms of the Creative Commons Attribution 4.0 License. Further distribution of this work must maintain attribution to the author(s) and the published article's title, journal citation, and DOI.

#### Introduction

The use of erbium-doped fiber amplifiers (EDFAs), in conjunction with polarization and wavelength multiplexing as well as coherent modulation, has enabled high capacity, long haul, and low latency communication systems that form the foundation of the modern Internet. However, the rapid increase in bandwidth demand driven by the proliferation of video streaming, social media platforms, and emerging technologies such as artificial intelligence, autonomous vehicles, and the Internet of Things necessitates further enhancement of the optical communication infrastructure [1]. A promising strategy to meet this demand is the exploitation of spectral regions beyond the conventional C+L band [2-5]. To this end, novel technologies such as hollow-core fibers [6–8] and frequency combs [9–11] in conjunction with space-division multiplexing [12] are being investigated. These approaches aim not only to expand the usable optical bandwidth but also to access previously untapped wavelength windows. However, realizing these capabilities requires the development of optical amplifiers that operate effectively within these extended spectral regions. Current rare-earth-ion-doped fiber amplifiers are constrained by fundamental material limits, motivating interest in alternative amplification methods.

<sup>&</sup>lt;sup>1</sup>Department of Microtechnology and Nanoscience, Chalmers University of Technology, 412 96

<sup>&</sup>lt;sup>2</sup>College of Electronics and Information Engineering, Sichuan University, Chengdu 610065, China

<sup>&</sup>lt;sup>3</sup>Currently with Solinide Photonics AB, 433 34 Partille, Sweden

vijaysh@chalmers.se

OPAs, which rely on nonlinear optical interactions, offer a compelling solution. Unlike EDFAs, OPAs can achieve a broadband gain that is independent of the material and is managed by dispersion engineering in a nonlinear medium [13–15]. Furthermore, due to phase matching conditions OPAs are inherently unidirectional and, when configured as phase-sensitive amplifiers, can theoretically achieve a noise figure as low as 0 dB [16]. OPAs are promising not only for classical communications but also for future quantum information systems, as they can generate and help in the detection of squeezed vacuum states [17]. Historically, OPAs have been explored using highly nonlinear fibers (HNLFs) [18–20] and periodically poled lithium niobate (PPLN) waveguides [21–23]. However, fiber-based OPAs have not been commercialized because of the complexities added while mitigating stimulated Brillouin scattering, as well as their requirement for long interaction lengths resulting from relatively large mode area and weak nonlinearity [24]. In addition, polarization mode dispersion makes the implementation of broadband amplifiers difficult [25]. PPLN-based OPAs, on the other hand, suffer from high temperature sensitivity, which limits their operational stability. Both platforms also face challenges related to limited scalability for volume manufacturing while nonlinear silicon nitride photonics has been demonstrated at the wafer scale [26,27].

The emergence of integrated photonics has revitalized interest in OPAs [28,29], offering a viable solution to the limitations that hindered their adoption in bulk counterparts. Integrated platforms, by virtue of their reduced mode area, alleviate the trade-offs among nonlinearity, pump power, and device length, while also enabling compact and scalable manufacturing [26,30,31]. A significant milestone was the demonstration of net positive gain from a continuous wave OPA on the low-loss Si<sub>3</sub>N<sub>4</sub> platform [32,33]. Although these demonstrations overcame propagation and coupling losses, the achieved gain was modest (< 5 dB) with a bandwidth of only several tens of nanometers and a black box NF of 3.7 dB, both considerably inferior to those offered by the HNLF-based OPA. In the broader field of integrated Kerr nonlinear optics, all prior works where the target is to maximize the accumulated nonlinear phase shift have used a strip waveguide geometry primarily to have higher nonlinearity [32–39]. More recently, a substantially broader amplification bandwidth of 300 nm was demonstrated on the same Si<sub>3</sub>N<sub>4</sub> platform by employing carefully engineered dispersion in a rib waveguide geometry [40]. This design, coupled with bending-induced modal filtering, enabled quasi-single mode operation [41]. However, the reported gain was low, and the impact of reduced nonlinearity on the achievable gain was not addressed. In this work, we aim to address the challenge of simultaneously achieving high net gain and broad bandwidth by analyzing the linear and nonlinear properties of strip and rib waveguide geometries fabricated on the Si<sub>3</sub>N<sub>4</sub> platform using an identical process.

Specifically, our study focuses on balancing key parameters that govern OPA performance, viz. scattering loss  $(\alpha)$ , group velocity dispersion coefficient  $(\beta_2)$ , effective nonlinear parameter  $(\gamma)$ , and the physical waveguide length  $(L_{\text{phy}})$ . We demonstrate that the rib waveguide exhibits improved gain or conversion efficiency (CE) near the zero dispersion wavelength due to reduced propagation loss [42] in spite of a lower nonlinear coefficient, while it requires approximately 30% longer physical length. As a result, the rib geometry also achieves a NF of approximately 0.4 dB better than that of the strip waveguide. Furthermore, we propose a practical meandered layout strategy to realize multi-meter long rib waveguides within a compact footprint. Finally, we evaluate the tolerance of  $\beta_2$  to height variations induced by fabrication in both geometries and find that the deviation from the design value remains similar across the strip and rib waveguides within a  $1\sigma$  fabrication uncertainty.

## 2. Linear and nonlinear properties of strip and rib waveguides

Figure 1(a) illustrates the cross-sectional geometries of the strip and rib waveguides, together with their respective simulated fundamental transverse electric (TE) modes. Notably, for geometries with comparable core dimensions and strong optical confinement, the rib waveguide exhibits

reduced modal overlap with the sidewalls and a larger mode area. This geometric distinction results in lower scattering losses [43] but also in a reduced nonlinear coefficient compared to the strip waveguide. As shown in Figs. 1(b) and (c), the most confined geometry exhibits the highest values of  $\alpha$  and  $\gamma$ , corresponding to the lower left corner for the strip geometry and the upper left corner for the rib. This unlocks a wider combination of loss and nonlinearity, facilitating the optimization of this critical trade-off, which is particularly beneficial when lower propagation loss is desired. Also, as expected,  $\beta_2$  decreases and transitions to anomalous values as the waveguide dimensions increase and the waveguide dispersion begins to dominate over the material dispersion.

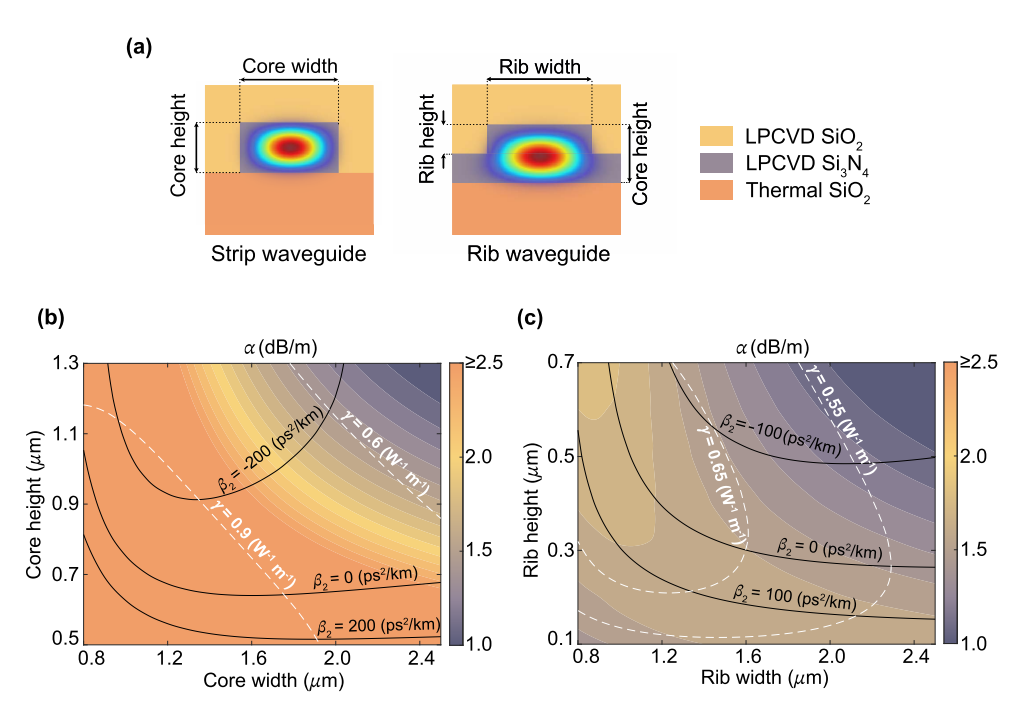


**Fig. 1.** (a) Cross section of strip and rib waveguide with simulated fundamental TE mode. Contour plot of scattering loss  $(\alpha)$ , second order dispersion  $(\beta_2)$ , and effective nonlinear coefficient  $(\gamma)$  for strip (b) and rib (c) waveguide. The simulations are done for a wavelength of 1550 nm and the fundamental TE mode. The core height in the simulations for the rib geometry is a sum of slab height  $(0.5 \ \mu m)$  and the rib height.

The scattering losses were calculated using the Payne–Lacey model for the strip geometry, and an extended formulation of the same model was applied to the rib configuration [43,44]. These simulations account for scattering contributions from the top, bottom, and sidewall interfaces. The characteristic surface roughness parameters root mean square (RMS) roughness ( $\sigma$ ) and correlation length ( $L_c$ ) were adopted from previously reported experimental measurements [45]. The simulated losses correspond to the fundamental TE mode at a wavelength of 1550 nm, with absorption losses assumed to be negligible. These scattering simulations are used to establish a comparative assessment between two distinct waveguide geometries, rather than to provide absolute predictions of scattering losses. Finally, the group velocity dispersion and the effective mode area were obtained using Lumerical MODE simulations, and  $\gamma$  was calculated using a nonlinear refractive index ( $n_2$ ) of  $2.4 \times 10^{-19}$  m<sup>2</sup>/W [46,47].

## 3. Optical parametric amplification in strip and rib waveguides

The peak gain occurring at a perfectly phase-matched wavelength of a pump-degenerate phase-insensitive amplifier (PIA) was calculated using the parameters derived in the previous section and the analytical equations from [48]. The results are presented in Figs. 2(a) and (b) for the strip and rib waveguides, respectively. In these calculations, the physical waveguide length was considered to be  $L_{\rm phy}=1/\alpha$ , which is also indicated in the respective plots. As in earlier experimental studies, we also use an on-chip pump power of 34 dBm at 1550 nm throughout our simulations [32,40]. For both waveguide geometries, the highest gain corresponds to regions with lowest scattering loss. In the case of the strip waveguide, the gain is mainly limited by  $\alpha$ , making

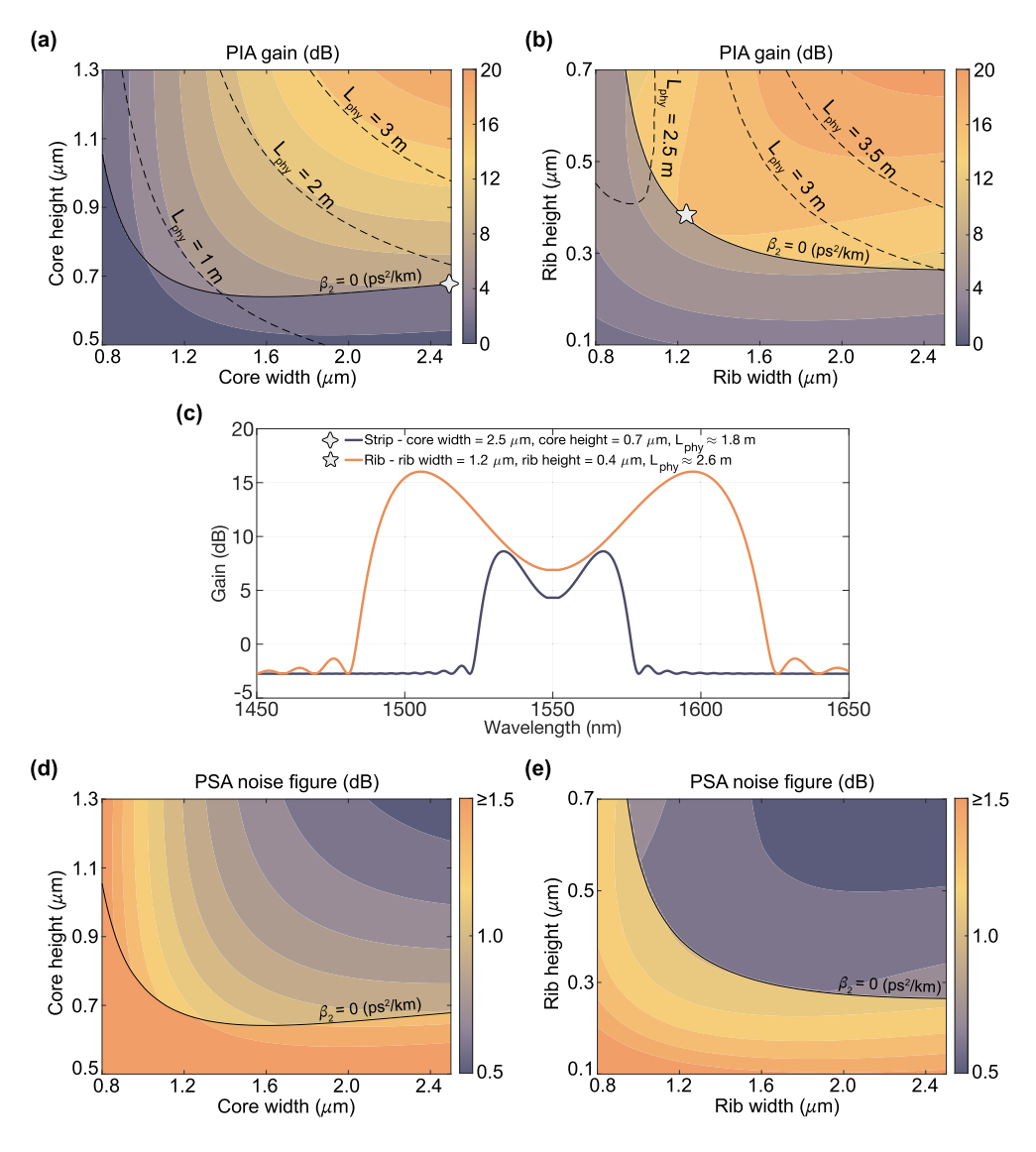


**Fig. 2.** Peak on-chip PIA gain,  $L_{\rm phy}$ , and  $\beta_2$  for strip (a) and rib (b) waveguide. Gain spectrum for the optimized strip and rib waveguides (c). On-chip PSA noise figure and  $\beta_2$  for strip (d) and rib (e) waveguide. A pump laser with a power of 34 dBm at a wavelength of 1550 nm is used in the simulation.

the scattering loss the dominant factor. In contrast, the rib waveguide exhibits a dependence on both scattering loss  $\alpha$  and nonlinear coefficient  $\gamma$ , allowing greater flexibility in engineering amplifier performance.

This design flexibility becomes particularly valuable in the realization of high-gain, broadband parametric amplifiers, where optimal performance is achieved near the zero-dispersion wavelength, that is, where the group velocity dispersion is slightly negative [40]. Under such conditions, the maximum gain for the strip waveguide is obtained at a waveguide height of approximately 0.7  $\mu$ m and a width of 2.5  $\mu$ m. For wider waveguides, the gain will plateau due to the saturation of the scattering loss at its minimum value [49]. In the rib geometry, where both  $\gamma$  and  $\alpha$  influence the gain, the optimal configuration is achieved with a rib width of 1.2  $\mu$ m and a height of 0.4  $\mu$ m for a fixed slab height of 0.5  $\mu$ m. Notably, this configuration offers up to 8 dB higher gain compared to the strip waveguide, despite having the same surface roughness. Moreover, across a wide range of rib dimensions, the achievable gain consistently exceeds that of the strip geometry for operation near the  $\beta_2 = 0$  condition. It can be seen in Fig. 2(c) that the longer length does not necessarily limit the bandwidth of the rib waveguide. Either of them can exhibit broadband behavior if the appropriate values of  $\beta_2$  and  $\beta_4$  are used. The slab height is fixed at 0.5  $\mu$ m, since reducing the height would enhance the confinement of higher order modes, increasing the risk of multi-mode operation and making it more difficult to achieve  $\beta_2 < 0$  [40]. On the other hand, a thicker slab would further decrease  $\gamma$  and necessitate an even longer device length to achieve high gain.

Further enhancement is possible through the use of a phase-sesitive amplifier (PSA) configuration, which can provide an additional 6 dB gain [20]. In the PSA regime, the rib waveguide also achieves a superior NF, approximately 0.4 dB lower than that of the strip waveguide. This is due to inherently higher gain in the rib waveguides while assuming that the coupling losses of both geometries are comparable. This is illustrated in Figs. 2(d) and (e), where the NF is calculated in a similar way to the gain above [48]. The achievable NF is also limited by the input loss of an optical amplifier. Since the rib waveguide uses only the slab as the edge coupler, the coupling loss of the rib and strip waveguides is comparable when a similar design and method of fabrication are used. The tapering down of the rib to transfer the mode into the slab layer does not add any significant loss [50]. The primary trade-off, however, is an increase in physical device length, with  $L_{\rm phy}$  extending from approximately 1.8 meters in the strip geometry to about 2.6 meters in the rib configuration. In addition, rib waveguides are less densely packed than strip waveguides because they also require a finite slab with a width of at least 6  $\mu$ m [40]. Nonetheless, as discussed in the following section, such long rib waveguides can be practically realized within compact chip footprints.

#### 4. Fabrication strategy for meter-long rib waveguides

A common strategy for the fabrication of long integrated waveguides is the use of concatenated Archimedean spiral layout [32,39,51]. This geometry requires careful optimization of design parameters such as the inner and outer radii, waveguide spacing, and slab width to mitigate crosstalk and maintain uniform dispersion and optical loss throughout the length of the waveguide. For the optimized rib waveguide considered in this work, a single spiral can yield a length of approximately 2.8 cm within a  $1 \times 1 \text{ mm}^2$  e-beam lithography writing field. However, when these spirals are stacked linearly in a single direction, as in traditional designs [32], the total length achievable on a standard 4-inch wafer is limited to approximately 1.6 meters, resulting in impractically large and unconventional chip dimensions, as illustrated in Fig. 3(a).

To address this limitation, we propose a meander-style spiral stacking, enabling the fabrication of waveguides with a target physical length ( $L_{phy}$ ) of 2.6 meters within a practical chip size of 20  $\times$  5 mm<sup>2</sup>. Notably, this layout strategy remains effective even with stepper-based UV lithography,

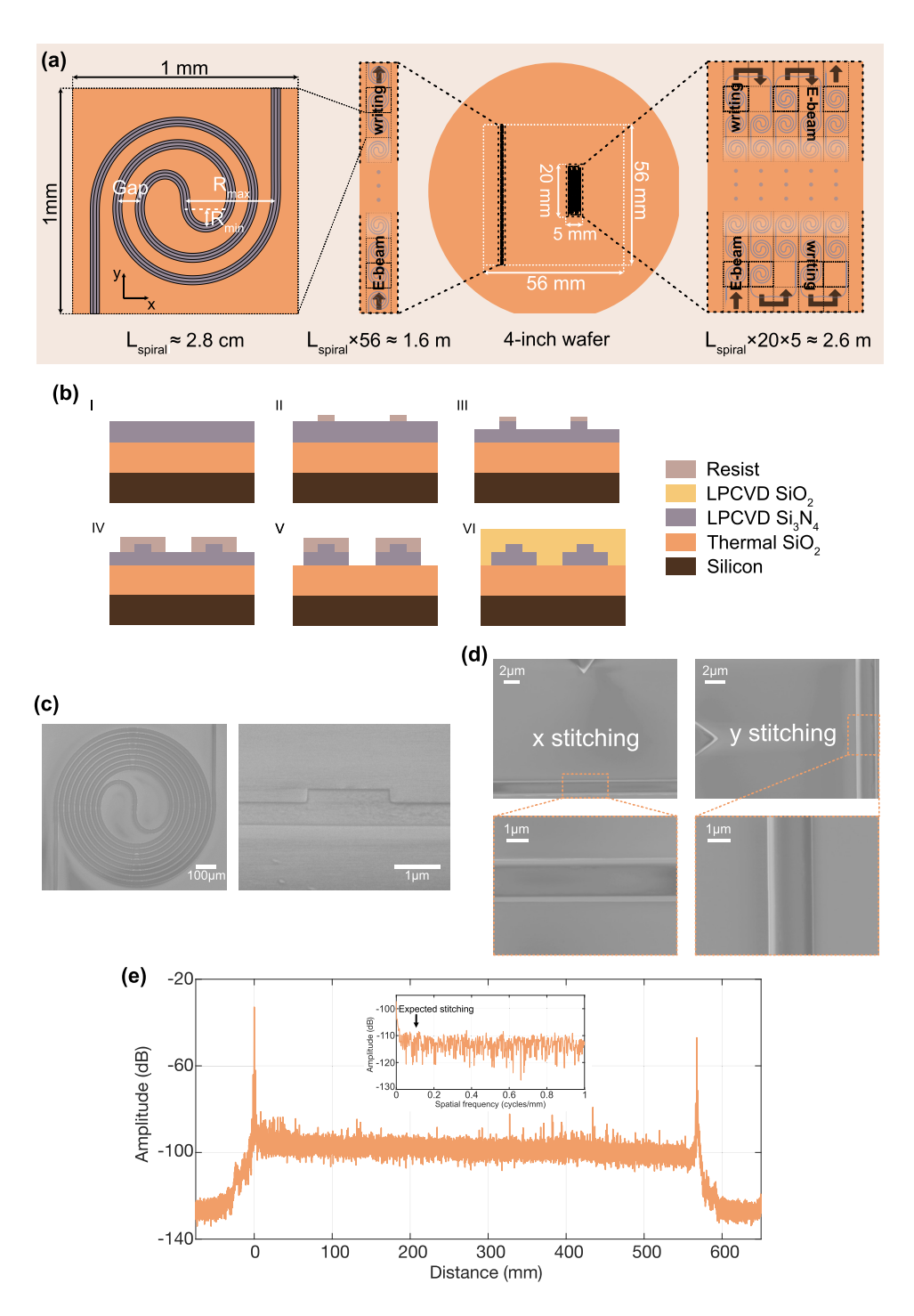


**Fig. 3.** (a) Meander approach for fabricating meter long rib waveguides. (b) Process flow for the fabrication of rib waveguide by subtractive processing. (c) SEM image of one spiral unit and its cross section. (d) SEM of stitching boundary in x and y direction. (e) OFDR plot for the fabricated test waveguide with a length of 0.56 m [40]. Inset: corresponding spatial frequency spectrum.

where the writing field or reticle size is substantially larger, as the outer diameter required to preserve single-mode operation is approximately 1100  $\mu$ m [40].

To validate the proposed layout and fabrication strategy, we implemented a prototype meander spiral with  $L_{\rm phy}\approx 0.56$  meters, as well as a chip size of  $29\times 3~{\rm mm}^2$ . It should be noted that this prototype is not optimized to utilize the maximum chip area. The rib waveguides were fabricated using a modified subtractive process, as shown in Fig. 3(b) [27,52]. The fabrication process begins with the thermal growth of a 3  $\mu$ m SiO<sub>2</sub> on a 4-inch silicon wafer. Crack barriers are then patterned into the oxide using optical lithography followed by a buffered oxide etch. Subsequently, low-pressure chemical vapor deposition (LPCVD) silicon nitride is deposited using thermal cycling, which further mitigates the risk of crack formation [53]. The rib layer of the waveguide is defined using e-beam lithography with a beam step size (BSS) of 4 nm. Exposure preparation is performed in GenISys BEAMER to accurately trace the optical path within each writing field and ensure continuity across adjacent fields. Due to the large device dimensions, proximity effect correction is applied independently for each writing field. Design considerations are made to ensure that features do not lie near field boundaries. Waveguide bends are designed to be adiabatic [51,54], and stitching boundaries are oriented along either the x- or y-axis to localize and isolate any potential stitching artifacts.

Following exposure, the pattern is transferred into the  $Si_3N_4$  layer using an inductively coupled plasma (ICP) etch with CHF<sub>3</sub> and O<sub>2</sub> chemistry. The etch duration is pre-calibrated to achieve the target rib height. The remaining resist is then stripped off and another layer is coated to etch down grooves in the slab layer. An ample amount of resist is used to cover the whole area of the devices so that uneven surfaces are uniformly covered. This is followed by a second e-beam exposure with a 10 nm BSS. A good alignment between the rib and the slab layer is achieved by employing a two-step alignment strategy. A global alignment is first performed with four markers spread around the wafer. Next, a local alignment is done with three markers before exposing the devices on each chip. The same ICP recipe is then employed to etch the slab layer. To mitigate wafer bowing, the Si<sub>3</sub>N<sub>4</sub> on the wafer backside is removed using an aggressive ICP etch. Then a high temperature anneal is performed after removing the resist at 1190°C for 180 minutes with Argon flow. Following the anneal, a 3  $\mu$ m thick SiO<sub>2</sub> top cladding is deposited via LPCVD in approximately 500 nm increments. Each layer is densified through intermediate anneals at 1100°C for 180 minutes in a nitrogen atmosphere. Finally, the chips are isolated using two sequential optical lithography and ICP etching steps: one for SiO<sub>2</sub> (using CF<sub>4</sub> and O<sub>2</sub>) and one for the Si substrate (using the Bosch process).

One of the challenges in meter-long waveguide fabrication based on e-beam lithography is to minimize the stitching error [32]. Here, we report that it is no longer necessary to actively compensate for the expected stitching error. We attribute this improvement to three key enhancements in our Raith EBPG5200 e-beam system. First, we implemented an improved calibration of the main-deflector distortion using a higher-resolution 51 × 51 measurement grid and randomized measurement order. Second, internal tool performance monitoring, including stitching accuracy evaluation, is now performed weekly to rapidly identify deviations. Finally, overlay test exposures provide an end-to-end verification of stitching performance. Test patterns consist of a cross written at a certain beam deflection and four surrounding rectangles written at a different deflection after a corresponding stage movement. The overlay error is measured as the deviation from the ideal relative position between the two structures. This procedure is repeated for various beam deflections and sample heights. The improved stitching is shown in the scanning electron microscope (SEM) images taken at the stitching boundaries between adjacent e-beam writing fields, as shown in Fig. 3(d). Markers etched into the Si<sub>3</sub>N<sub>4</sub> layer indicate the field boundaries, and the magnified image confirms well-aligned stitching without discontinuities. Furthermore, optical frequency domain reflectometry (OFDR) measurements, presented in Fig. 3(e) [40], do not exhibit periodic reflection peaks indicative of stitching-induced index

discontinuities. In the inset, we plot the spatial frequency spectrum by doing a Fourier transform of the OFDR measurement. We also did not observe any peak at around 0.12 cycles/mm, which corresponds to one spiral length of about 8.2 mm. The observed random reflection peaks are attributed to surface contaminants, which can be minimized through an improved cleaning methodology. The measured propagation loss was 2.5 dB/m for this rib waveguide with a height of 0.3  $\mu$ m, a width of 1.9  $\mu$ m, and a slab height of 0.3  $\mu$ m.

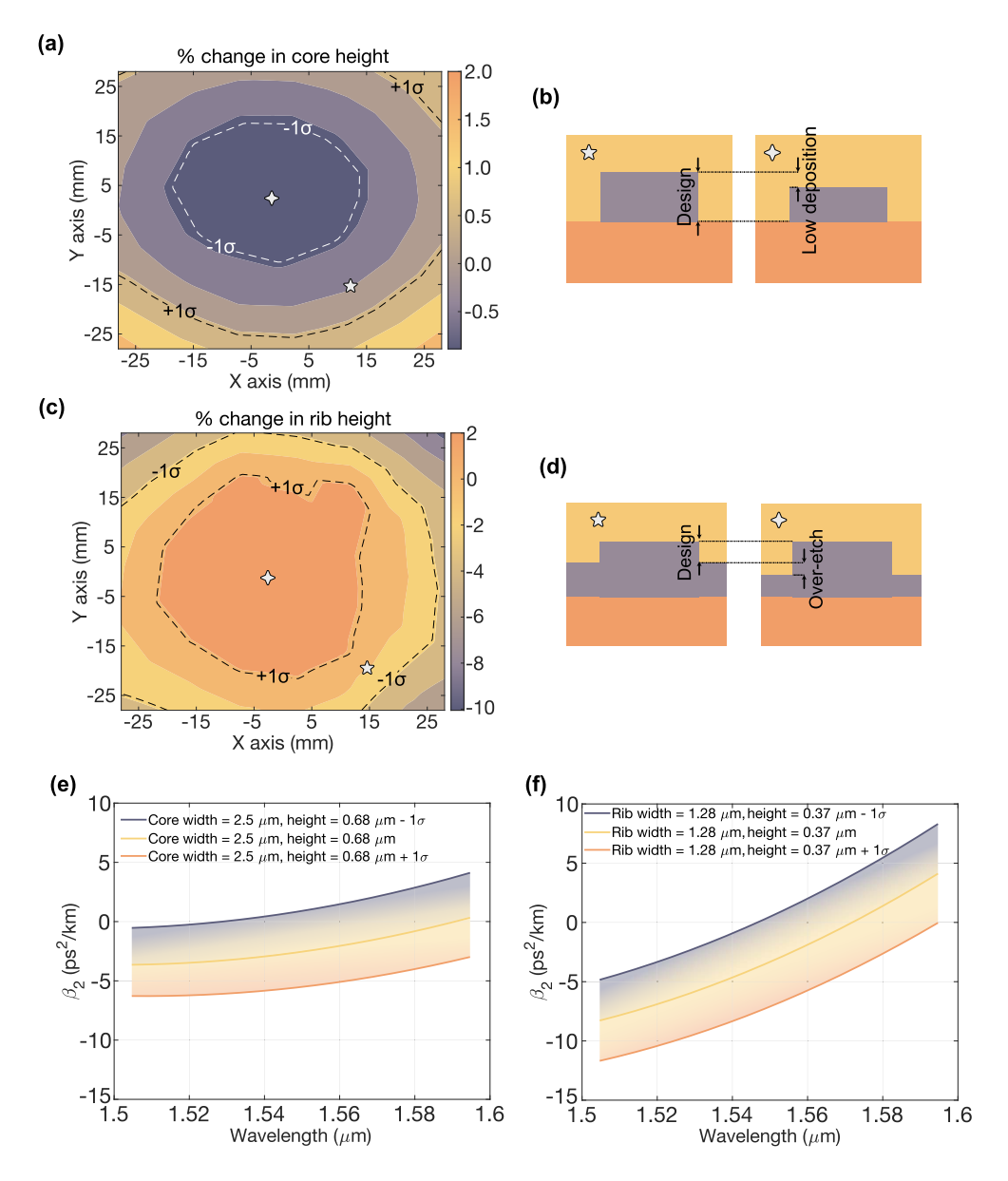


**Fig. 4.** Percentage change in core (a) and rib (c) height over a 4-inch wafer and its  $1\sigma$  variation. The height variation is measured by ellipsometry. Origin of height variation for strip (b) and rib (d) waveguide. The resulting  $\beta_2$  variation within  $1\sigma$  deviation for strip (e) and rib (f) structure.

## 5. Analysis of fabrication tolerance

Achieving broadband amplification requires precise control over waveguide dispersion, which makes it essential to characterize dimensional variations across the wafer. In subtractive processing, maintaining uniformity in the waveguide width is generally more feasible than achieving a consistent height. This distinction is critical because  $\beta_2$  is significantly more sensitive to variations in the waveguide height than to the width, cf. Figure 1.

For strip waveguides, the height variation is constrained by the deposition uniformity of the low pressure chemical vapor deposition (LPCVD) Si<sub>3</sub>N<sub>4</sub> layer. In contrast, rib waveguide height variation is influenced by both the uniformity of material deposition and the inductively coupled plasma (ICP) etching process used to define the rib, as shown in Fig. 4. While the ICP etch initially compensates for deposition non-uniformity, it eventually becomes the primary source of height variation across the wafer. Consequently, rib waveguides exhibit a higher percentage height variation compared to strip waveguides. If we want to target a specific value of  $\beta_2 \approx -2.5$ ps<sup>2</sup>/km for broadband amplification, the impact on group velocity dispersion remains comparable for both geometries, despite the higher percentage variation. As illustrated in Figs. 4(e) and (f) with approximately  $\pm 3 \text{ ps}^2/\text{km}$  within a  $1\sigma$  deviation from ideal core and rib height, respectively. This behavior arises because the rib waveguide has a smaller nominal height, so even a higher percentage change introduces a small absolute change in the rib height, which has a reduced impact on the overall dispersion. In addition, the sensitivity of  $\beta_2$  to rib height decreases further as the rib width is reduced, as previously shown in Fig. 1(c). This analysis indicates that the optimized strip and rib waveguides have similar fabrication tolerances when targeting a specific value of  $\beta_2$ . Finally, it is worth noting that the etch rate uniformity in the ICP process can be further improved by optimizing process parameters such as the distance between the plasma source and substrate or by utilizing a larger plasma chamber, thereby reducing fabrication-induced variability in dispersion.

## 6. Conclusion

In this work, we have numerically investigated the interplay between the nonlinear coefficient and the scattering loss to realize a high-gain broadband OPA on the Si<sub>3</sub>N<sub>4</sub> integrated photonics platform. Our analysis demonstrates that rib waveguides offer a more favorable trade-off than strip waveguides, primarily due to their lower scattering loss. However, this advantage comes at the cost of requiring longer physical lengths to achieve comparable nonlinear interaction. To address this, we proposed and experimentally validated a meander-style spiral layout can enable the fabrication of rib waveguides exceeding 2.5 meters in length within a practical chip footprint. We also showed that active stitching compensation can be avoided using electron-beam lithography-based subtractive processing, with no observable reflection artifacts. Furthermore, we confirmed that dimensional variability in the rib waveguides does not significantly compromise the ability to target specific dispersion values. Crucially, we optimize the waveguide design for the highest accumulated nonlinear phase shift, which serves as a more relevant figure of merit than the scattering loss  $\alpha$  and/or the effective nonlinear parameter  $\gamma$ . As such, the design principles demonstrated here are not limited to Si<sub>3</sub>N<sub>4</sub> or the specific case of OPA, but are broadly applicable across various devices based on integrated Kerr nonlinear platforms. This includes, for example, wavelength conversion in InGaAs [36], signal regeneration in Si [55], and OPA in GaP [38]. To summarize, the rib waveguide geometry opens up a versatile design space for optimizing nonlinear integrated photonic devices, enabling more efficient and broadband integrated parametric devices.

Funding. Vetenskapsrådet (2020-00453, 2015-00535, 2022-06575); Knut och Alice Wallenbergs Stiftelse (KAW Scholar - Peter A. Andrekson).

Acknowledgment. This work was performed in part at Myfab Chalmers.

**Disclosures.** Victor Torres-Company and Marcello Girardi are co-founders and shareholders of Solinide Photonics AB.

**Data availability.** Data underlying the results presented in this paper are available in Ref. [56]

#### References

- 1. E. Agrell, M. Karlsson, F. Poletti, et al., "Roadmap on optical communications," J. Opt. 26(9), 093001 (2024).
- T. Hoshida, V. Curri, L. Galdino, et al., "Ultrawideband Systems and Networks: Beyond C + L-Band," Proc. IEEE 110(11), 1725–1741 (2022).
- S. Escobar-Landero, X. Zhao, D. L. Gac, et al., "Demonstration and Characterization of High-Throughput 200.5 Tbit/s S+C+L Transmission over 2x100 PSCF Spans," J. Lightwave Technol. 41(12), 3668–3673 (2023).
- 4. B. J. Puttnam, R. S. Luis, Y. Huang, *et al.*, "301 Tb/s E, S, C+L-band transmission over 212 nm bandwidth with E-band bismuth-doped fiber amplifier and gain equalizer," in *49th European Conference on Optical Communications* (2023), pp. 1674–1677.
- M. Abe, S. Shimizu, T. Kazama, et al., "Periodically Poled Lithium-niobate-based Wavelength Converters for Waveband Extension to U-Band and Beyond," J. Lightwave Technol. 43(13), 6335–6341 (2025).
- Y. Chen, M. Petrovich, E. N. Fokoua, et al., "Hollow Core DNANF Optical Fiber with <0.11 dB/km Loss," in Optical Fiber Communication Conference (Optica Publishing Group, 2024), paper Th4A.8.
- 7. D. McCulloch, K. R. H. Bottrill, Y. Jung, *et al.*, "Simultaneous Power and Data Transmission over 1.21 km of Nested Antiresonant Nodeless Fibre," in *50th European Conference on Optical Communication* (2024), pp.1748–1751.
- 8. M. Petrovich, E. Numkam Fokoua, Y. Chen, *et al.*, "First broadband optical fibre with an attenuation lower than 0.1 decibel per kilometre," arXiv (2025).
- B. J. Puttnam, R. S. Luís, W. Klaus, et al., "2.15 Pb/s transmission using a 22 core homogeneous single-mode multi-core fiber and wideband optical comb," in European Conference on Optical Communication (2015), paper PDP 3–1.
- A. A. Jørgensen, D. Kong, M. R. Henriksen, et al., "Petabit-per-second data transmission using a chip-scale microcomb ring resonator source," Nat. Photonics 16(11), 798–802 (2022).
- 11. B. Corcoran, A. Mitchell, R. Morandotti, *et al.*, "Optical microcombs for ultrahigh-bandwidth communications," Nat. Photonics **19**(5), 451–462 (2025).
- B. J. Puttnam, G. Rademacher, and R. S. Luís, "Space-division multiplexing for optical fiber communications," Optica 8(9), 1186–1203 (2021).
- M. E. Marhic, N. Kagi, T.-K. Chiang, et al., "Broadband fiber optical parametric amplifiers," Opt. Lett. 21(8), 573–575 (1996).
- L. Provino, A. Mussot, E. Lantz, et al., "Broadband and flat parametric amplifiers with a multisection dispersiontailored nonlinear fiber arrangement," J. Opt. Soc. Am. B 20(7), 1532–1537 (2003).
- J. M. C. Boggio, J. D. Marconi, S. R. Bickham, et al., "Spectrally flat and broadband double-pumped fiber optical parametric amplifiers," Opt. Express 15(9), 5288–5309 (2007).
- 16. C. M. Caves, "Quantum limits on noise in linear amplifiers," Phys. Rev. D 26(8), 1817–1839 (1982).
- 17. R. Nehra, R. Sekine, L. Ledezma, et al., "Few-cycle vacuum squeezing in nanophotonics," Science 377(6612), 1333–1337 (2022).
- 18. J. Hansryd, P. Andrekson, M. Westlund, *et al.*, "Fiber-based optical parametric amplifiers and their applications," IEEE J. Sel. Top. Quantum Electron. **8**(3), 506–520 (2002).
- S. Radic, C. McKinstrie, A. Chraplyvy, et al., "Continuous-wave parametric gain synthesis using nondegenerate pump four-wave mixing," IEEE Photonics Technol. Lett. 14(10), 1406–1408 (2002).
- Z. Tong, C. Lundström, P. A. Andrekson, et al., "Towards ultrasensitive optical links enabled by low-noise phase-sensitive amplifiers," Nat. Photonics 5(7), 430–436 (2011).
- 21. M. Asobe, T. Umeki, and O. Tadanaga, "Phase sensitive amplification with noise figure below the 3 dB quantum limit using CW pumped PPLN waveguide," Opt. Express 20(12), 13164–13172 (2012).
- 22. T. Kazama, T. Umeki, S. Shimizu, et al., "Over-30-dB gain and 1-dB noise figure phase-sensitive amplification using a pump-combiner-integrated fiber I/O PPLN module," Opt. Express 29(18), 28824–28834 (2021).
- S. Shimizu, T. Kobayashi, T. Kazama, et al., "PPLN-Based Optical Parametric Amplification for Wideband WDM Transmission," J. Lightwave Technol. 40(11), 3374–3384 (2022).
- 24. R. Larsson, R. U. Weerasuriya, and P. A. Andrekson, "Ultralow-noise preamplified optical receiver using conventional single-wavelength transmission," Optica 11(11), 1497–1502 (2024).
- Q. Lin and G. P. Agrawal, "Effects of polarization-mode dispersion on fiber-based parametric amplification and wavelength conversion," Opt. Lett. 29(10), 1114–1116 (2004).
- J. Liu, G. Huang, R. N. Wang, et al., "High-yield, wafer-scale fabrication of ultralow-loss, dispersion-engineered silicon nitride photonic circuits," Nat. Commun. 12(1), 2236 (2021).
- M. Girardi, Ó. B. Helgason, C. H. López-Ortega, et al., "Superefficient microcombs at the wafer level," Opt. Express 33(13), 27451–27460 (2025).
- M. A. Foster, A. C. Turner, J. E. Sharping, et al., "Broad-band optical parametric gain on a silicon photonic chip," Nature 441(7096), 960–963 (2006).
- M. R. Lamont, B. Luther-Davies, D.-Y. Choi, et al., "Net-gain from a parametric amplifier on a chalcogenide optical chip," Opt. Express 16(25), 20374–20381 (2008).

- 30. L. Thiel, J. E. Castro, T. J. Steiner, *et al.*, "Wafer-scale fabrication of InGaP-on-insulator for nonlinear and quantum photonic applications," Appl. Phys. Lett. **125**(13), 131102 (2024).
- 31. C. J. Xin, S. Lu, J. Yang, *et al.*, "Wavelength-accurate and wafer-scale process for nonlinear frequency mixers in thin-film lithium niobate," Commun. Phys. **8**(1), 136 (2025).
- 32. Z. Ye, P. Zhao, K. Twayana, *et al.*, "Overcoming the quantum limit of optical amplification in monolithic waveguides," Sci. Adv. 7(38), eabi8150 (2021).
- 33. J. Riemensberger, N. Kuznetsov, J. Liu, *et al.*, "A photonic integrated continuous-travelling-wave parametric amplifier," Nature **612**(7938), 56–61 (2022).
- 34. K. J. A. Ooi, D. K. T. Ng, T. Wang, *et al.*, "Pushing the limits of CMOS optical parametric amplifiers with USRN:Si7N3 above the two-photon absorption edge," Nat. Commun. **8**(1), 13878 (2017).
- 35. M. Pu, H. Hu, L. Ottaviano, *et al.*, "Ultra-Efficient and Broadband Nonlinear AlGaAs-on-Insulator Chip for Low-Power Optical Signal Processing," Laser Photonics Rev. **12**(12), 1800111 (2018).
- D. Kong, Y. Liu, Z. Ren, et al., "Super-broadband on-chip continuous spectral translation unlocking coherent optical communications beyond conventional telecom bands," Nat. Commun. 13(1), 4139 (2022).
- A. Ayan, J. Liu, T. J. Kippenberg, et al., "Towards efficient broadband parametric conversion in ultra-long Si<sub>3</sub>N<sub>4</sub> waveguides," Opt. Express 31(24), 40916–40927 (2023).
- N. Kuznetsov, A. Nardi, J. Riemensberger, et al., "An ultra-broadband photonic-chip-based parametric amplifier," Nature 639(8056), 928–934 (2025).
- S. Ishimura, A. E. Elfiqi, T. Kan, et al., "Silicon-nitride photonic integrated waveguide for dual-polarization traveling-wave four-wave-mixing applications," Opt. Express 33(9), 19546–19557 (2025).
- P. Zhao, V. Shekhawat, M. Girardi, et al., "Ultra-broadband optical amplification using nonlinear integrated waveguides," Nature 640(8060), 918–923 (2025).
- 41. E. A. J. Marcatili, "Bends in optical dielectric guides," The Bell Syst. Tech. J. 48(7), 2103-2132 (1969).
- P. Dong, W. Qian, S. Liao, et al., "Low loss shallow-ridge silicon waveguides," Opt. Express 18(14), 14474–14479 (2010).
- K. P. Yap, A. Delage, J. Lapointe, et al., "Correlation of Scattering Loss, Sidewall Roughness and Waveguide Width in Silicon-on-Insulator (SOI) Ridge Waveguides," J. Lightwave Technol. 27(18), 3999–4008 (2009).
- 44. F. P. Payne and J. P. R. Lacey, "A theoretical analysis of scattering loss from planar optical waveguides," Opt. Quantum Electron. 26(10), 977–986 (1994).
- S. Roberts, X. Ji, J. Cardenas, et al., "Measurements and Modeling of Atomic-Scale Sidewall Roughness and Losses in Integrated Photonic Devices," Adv. Opt. Mater. 10(18), 2102073 (2022).
- 46. G. P. Agrawal, Nonlinear Fiber Optics (Academic Press, 2023), 6th ed.
- K. Ikeda, R. E. Saperstein, N. Alic, et al., "Thermal and Kerr nonlinear properties of plasma-deposited silicon nitride/silicon dioxide waveguides," Opt. Express 16(17), 12987–12994 (2008).
- P. Zhao, M. Karlsson, and P. A. Andrekson, "Low-Noise Integrated Phase-Sensitive Waveguide Parametric Amplifiers," J. Lightwave Technol. 40(1), 128–135 (2022).
- 49. Y. Sun, Z. Ye, R. V. Laer, et al., "Low-loss dispersion-engineered silicon nitride waveguides coated with a thin blanket layer," in *Conference on Lasers and Electro-Optics* (Optica Publishing Group, 2022), paper JW3B.183.
- 50. S. K. Selvaraja, W. Bogaerts, P. Absil, et al., "Record low-loss hybrid rib/wire waveguides for silicon photonic circuits," in *Group IV Photonics*, 7th International conference, Proceedings (IEEE, 2010), p. 3.
- T. Chen, H. Lee, J. Li, et al., "A general design algorithm for low optical loss adiabatic connections in waveguides," Opt. Express 20(20), 22819–22829 (2012).
- 52. Z. Ye, K. Twayana, P. A. Andrekson, *et al.*, "High-Q Si<sub>3</sub>N<sub>4</sub> microresonators based on a subtractive processing for Kerr nonlinear optics," Opt. Express **27**(24), 35719–35727 (2019).
- 53. J. S. Levy, A. Gondarenko, M. A. Foster, *et al.*, "CMOS-compatible multiple-wavelength oscillator for on-chip optical interconnects," Nat. Photonics 4(1), 37–40 (2010).
- Z. Ye, F. Lei, K. Twayana, et al., "Integrated, Ultra-Compact High-Q Silicon Nitride Microresonators for Low-Repetition-Rate Soliton Microcombs," Laser Photonics Rev. 16(3), 2100147 (2022).
- R. Salem, M. A. Foster, A. C. Turner, et al., "Signal regeneration using low-power four-wave mixing on silicon chip," Nat. Photonics 2(1), 35–38 (2008).
- V. Shekhawat, P. Zhao, N. Lindvall, et al., "Rib waveguides for Kerr nonlinear optics," Zenodo (2025), https://doi.org/10.5281/zenodo.17184299.